Journal Pre-proof

Synergistic effect of tri-doping with Mn, Ge, and Bi and thermoelectric enhancement of SnTe induced by grain boundary engineering and nanostructuring

Donghyun Shin, U.Sandhya Shenoy, Hyejeong Choi, Joseph Ngugi Kahiu, Eun-Ji Meang, Kwi-Il Park, Kwan-Ho Park, D.Krishna Bhat, Ho Seong Lee

PII: S2352-8478(25)00109-1

DOI: https://doi.org/10.1016/j.jmat.2025.101119

Reference: JMAT 101119

To appear in: *Journal of Materiomics*

Received Date: 30 April 2025

Revised Date: 14 July 2025

Accepted Date: 14 July 2025

Please cite this article as: Shin D, Shenoy US, Choi H, Kahiu JN, Meang E-J, Park K-I, Park K-H, Bhat DK, Lee HS, Synergistic effect of tri-doping with Mn, Ge, and Bi and thermoelectric enhancement of SnTe induced by grain boundary engineering and nanostructuring, *Journal of Materiomics*, https://doi.org/10.1016/j.jmat.2025.101119.

Grainboundary engineering and Nanostructuring

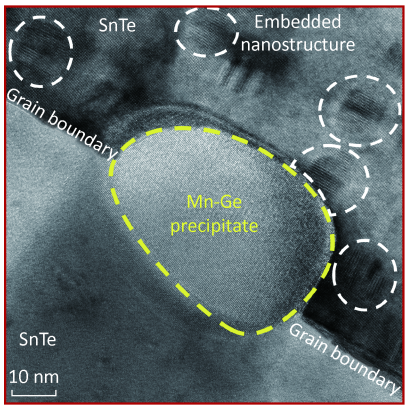

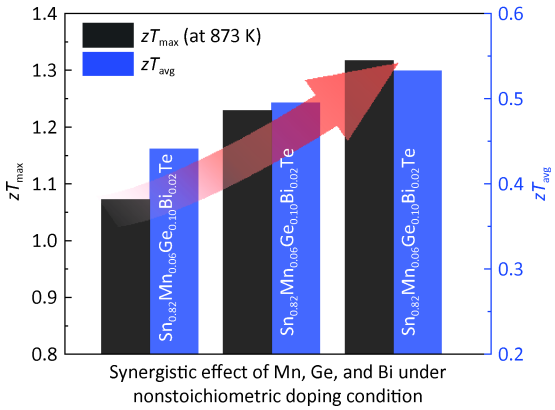

Synergistic effect of Mn, Ge, and Bi under nonstoichiometric doping condition

Synergistic effect of tri-doping with Mn, Ge, and Bi and thermoelectric enhancement of SnTe induced by grain boundary engineering and nanostructuring

Donghyun Shin,[a,b,c] U.Sandhya Shenoy,[d] Hyejeong Choi,[a,c] Joseph Ngugi Kahiu,[a,b] Eun-Ji Meang,[a,e] Kwi-Il Park,[a,b,c] Kwan-Ho Park,[e] D. Krishna Bhat,[f] Ho Seong Lee*[a,b,c]

[a] Department of Materials Science and Metallurgical Engineering, Kyungpook National University, 80 Daehak-ro, Buk-gu, Daegu, 41566, Republic of Korea.

[b] Research Institute of Automative Parts and Materials, Kyungpook National University, 80 Daehak-ro, Buk-gu, Daegu, 41566, Republic of Korea.

[c] Innovative Semiconductor Education and Research Center for Future Mobility, Kyungpook National University, 80 Daehak-ro, Buk-gu, Daegu 41566, Republic of Korea

[d] Department of Materials Science and Engineering,Institute of Engineering and Technology, Srinivas University, Mukka - 574146, Mangalore, Karnataka, India

[e] Department of Thermoelectric power generation, DAEYANG Co., Ltd., C-dong, 34 SeongSeo-ro 71-gil, Dalseo-gu, Daegu, 42703, Republic of Korea

[f] National Institute of Technology Karnataka, Surathkal Srinivasnagar - 575025, Mangalore, Karnataka, India

* Corresponding author, Email: hs.lee@knu.ac.kr

Abstract

In this study, we propose grain boundary engineering and nanostructuring to enhance the thermoelectric performance of SnTe through tri-doping with Mn, Ge, and Bi. The synergistic effects on the band structure were analyzed through DFT calculations and validated through a series of doping experiments with each dopant. The nonstoichiometrically tri-doped sample exhibits a unique microstructure, characterized by Mn-Ge precipitates along the grain boundaries and coherently embedded nanostructures within the matrix. These microstructural features, combined with the effects of each dopant, synergistically enhanced the thermoelectric properties, yielding a maximum zT of 1.32 at 873 K. The thermoelectric generator exhibited a maximum output power of 661 μW at ΔT = 485 K, confirming its viability for mid-temperature thermoelectric applications.

Keyword: Grain boundary engineering, nano structuring, tri-doping, thermoelectric materials, SnTe.

1. Introduction

Thermoelectric generators (TEG) are a promising technology that directly converts heat into electricity, enabling the recovery of waste heat from energy inefficiencies in production, transport, and commercial usage [1–3]. In addition to being cost-effective and eco-friendly, TEGs operate noiselessly and have no moving parts, making them highly reliable [4,5]. To achieve high energy conversion efficiency in TEGs, thermoelectric materials with a high zT value are essential [6,7]. zT is the dimensionless Figure of merit used to evaluate the performance of thermoelectric materials, expressed as $zT = S^2\sigma T/\kappa$, where S, σ, κ, T represent the Seebeck coefficient, electrical conductivity, total thermal conductivity, and absolute temperature, respectively [8,9].

Thermoelectric materials with high energy conversion efficiency, such as skutterudites [10,11], half-Heusler compounds [12–14], and metal chalcogenides [15–20], are being actively studied by research groups worldwide. Among these, group-IV chalcogenides have demonstrated high performance as thermoelectric materials for mid-temperature applications [21–23]. SnTe is a group-IV chalcogenide thermoelectric material that is less expensive than GeTe and, unlike PbTe, does not contain toxic elements [24]. However, SnTe has a low Seebeck coefficient and high electronic thermal conductivity, resulting in a low zT value ($zT < 0.5$) [25]. This low performance is linked to the intrinsically high carrier concentration of SnTe-based thermoelectric materials (10^{20}–10^{21} cm^{-3}), which originates from a high density of intrinsic Sn vacancies [26,27]. Sn vacancies are easily generated in the SnTe compound, even under Sn-rich conditions [28]. The low Seebeck coefficient of SnTe is also related to the energy separation ($\Delta E_{L\text{-}\Sigma}$) and the small bandgap in its band structure [29]. The conduction band

minimum and the valence band maximum of SnTe are located at the L point of the Brillouin zone, giving it a small direct bandgap of around 0.18 eV [30]. This narrow bandgap leads to the easily occurring bipolar effect, which reduces the Seebeck coefficient while increasing thermal conductivity, ultimately deteriorating thermoelectric performance at high temperatures [31]. Additionally, the band structure of SnTe has an energy difference ($\Delta E_{L\text{-}\Sigma}$) of approximately 0.3 eV [25]. So, narrowing this energy difference is essential to enable contributions from the heavy Σ valence band and improve the Seebeck coefficient [25,32].

To address these issues, composition control has been widely utilized to suppress vacancy formation through the Sn self-compensation [33,34]. Additionally, multielement doping has been proposed to enhance thermoelectric performance by optimizing electronic and thermal transport properties [35–39]. For band structure modification, In [40] and Zn [41] are known to introduce a resonance state near the Fermi level, and Cd [33], Ca [42], and Mg [43] are known to introduce a valence band convergence effect. Mn doping in SnTe has been reported to induce both effects [44]. Ge doping in SnTe is reported to reduce lattice thermal conductivity while increasing the solubility limit of Mn [39,45]. In previous reports, Mn has been shown to exhibit a solubility range of 9%–15% (in mole) in SnTe [46–48], whereas Ge has been reported to have a solubility limit above 30% [49,50]. Nonetheless, several studies have reported the inevitable formation of precipitates when Mn or Ge is doped into SnTe [38,44,51]. Previous studies reported that these precipitates can reduce lattice thermal conductivity, but they also increase the carrier concentration due to donor loss, which deteriorates the thermoelectric properties [44,51,52]. Nonstoichiometric SnTe samples with various Mn and Ge doping levels were synthesized, and their thermoelectric properties were

investigated, as detailed in the Supplementary Material. Among them, the $Sn_{0.90}Mn_{0.06}Ge_{0.10}Te$ composition exhibited the highest thermoelectric performance. Bi doping in SnTe has been reported to modify the electronic band structure [53,54] and effectively reduce the carrier concentration [55]. Based on these findings, Bi was introduced as an aliovalent dopant at Sn sites in $Sn_{0.90}Mn_{0.06}Ge_{0.10}Te$ to further enhance its thermoelectric properties by simultaneously optimizing the carrier concentration and inducing additional point defects.

This study presents a grain boundary engineering and nanostructuring approach by employing a nonstoichiometric tri-doping method to enhance the thermoelectric performance of SnTe. We investigated the effect of each dopant on the thermoelectric properties under nonstoichiometric doping conditions and assessed their combined contribution to performance improvement. Herein, the tri-doping strategy enabled the modulation of anisotropic valence bands and the reduction of lattice thermal conductivity, effects that have also been reported in previous entropy engineering studies on SnTe [56,57]. In addition, a nonstoichiometric doping approach was employed to mitigate donor loss due to secondary phase formation and to promote the formation of a unique microstructure. Mn, Ge, and Bi have been studied for their distinct roles in SnTe: Mn primarily modifies the band structure [58], Ge reduces lattice thermal conductivity [39], and Bi fine-tunes electrical properties [59]. However, their combined effects have not been explored. These synergistic effects lead to a zT value of 1.32 at 873 K in the nonstoichiometrically tri-doped sample ($Sn_{0.88}Mn_{0.06}Ge_{0.10}Bi_{0.02}Te$), which is 23% higher than that of the conventionally tri-doped sample ($Sn_{0.82}Mn_{0.06}Ge_{0.10}Bi_{0.02}Te$). The proposed strategy in this study provides a promising pathway for developing high-efficiency thermoelectric materials for mid-temperature applications.

2. Experimental section

2.1 Reagents

Tin (shot, 99.999%), tellurium (lump, 99.999%), germanium (pieces, 99.999%), and bismuth (shot, 99.99%) from Alfa Aesar and manganese (powder, 99.9%) from YAKURI were used for synthesis. These materials were used as received, without any additional purifications.

2.2 Sample synthesis

In this study, compositions of $Sn_{1-y-z}Mn_xGe_yBi_zTe$ (x = 0, 0.05, 0.06, 0.07, 0.10; y = 0, 0.05, 0.10, 0.15; z = 0, 0.01, 0.02, 0.03) were established for the experiments. The reagents were weighed according to the specified ratios and then loaded into quartz tubes. The quartz tubes were evacuated to 10^{-3} torr, purged with Ar gas five times, and sealed using an oxygen cutter. The ampoules were heated to 1173 K for 16 hours in a rocking furnace and then quenched in cold water. The quenched ingots were annealed at 873 K for 48 h in a box furnace to ensure homogeneity. The resulting ingots were hand-milled to a size below 45 μm and then sintered using uniaxial hot pressing for 1 h at 823 K under 80 MPa.

2.3 Phase characterization

X-ray diffraction (XRD) was conducted using a EMPYREAN diffractometer (Malvern Panalytical, UK) with Cu K_α radiation (λ = 1.5425 Å). Measurements were conducted at room temperature over an angular range of 20° to 80° with 0.02° increments. Microstructural analysis

was carried out using a JSM-IT710HR field emission scanning electron microscope (FE-SEM, JEOL, japan) equipped with an Ultim Max100 energy dispersive X-ray spectroscopy (EDS, Oxford Instruments, UK). Additionally, a JXA-8530F field emission electron probe micro analyzer (FE-EPMA, JEOL, japan) with wavelength dispersive X-ray spectroscopy (WDS) was employed to determine the precise chemical composition of polished sample surfaces. The microstructure and atomic defects were analyzed with a Titan G2 ChemiSTEM Cs probe field emission transmission electron microscope (FE-TEM, FEI Company, USA) operated at 200 kV.

2.4 Thermoelectric measurement

Electrical properties were measured from room temperature to 873 K using a Seebeck coefficient and resistivity measurement system (BS-1, Blue-Sys, Korea). To determine the carrier concentration and mobility at room temperature, a four-probe Hall measurement system (HMS-3000, Ecopia, Korea) was utilized. The Hall effect measurement was performed using the van der Pauw method under a reversible magnetic field of 0.55 T. The bandgap was determined by extrapolating a Tauc plot obtained through Fourier transform infrared spectroscopy (FT-IR, PerkinElmer, US), following equations from previous studies [60–62]. Thermal diffusivity was measured using a laser flash analyzer (LFA467-HT, NETZSCH, Germany), with an instrument error margin of less than 3%. Using Archimedes' method, the density (ρ) was measured, and all samples were confirmed to achieve over 99% of the theoretical density. The specific heat capacity was calculated using the Dulong–Petit law $C_{\mathrm{P}} = 3R/M$, where R is the gas constant and M is the molar mass. The electronic thermal

conductivity was calculated using the Wiedemann–Franz law. The Lorenz number (L) was determined using the equation $L = 1.5 + \exp\left(\frac{-|S|}{116}\right)$ [63].

2.5 Computational details

The electronic structure and density of states (DOS) was obtained using Quantum ESPRESSO package based on first principles density functional theory [64]. To simulate the doped and undoped SnTe compositions a $\sqrt{2}\times\sqrt{2}\times2$ supercell containing 32 atoms were employed. To take into consideration the spin orbit coupling in the atoms of high atomic mass relativistic pseudopotentials of Perdew, Burke, and Ernzerhof (PBE) functional type were used [65]. $4d^{10}\ 5s^2\ 5p^2$, $3s^2\ 3p^6\ 4s^2\ 3d^5$, $4s^2\ 4p^2$, $5d^{10}\ 6s^2\ 6p^3$, $4d^{10}\ 5s^2\ 5p^4$ were considered as valence electrons for Sn, Mn, Ge, Bi and Te, respectively through the use of ultrasoft pseudopotentials. The total energies were determined for the fully relaxed structures. A 50 Ry energy cut off and 500 Ry charge density cutoff values were used to truncate the plane wave basis representing the wave functions. A k mesh of 1960 points was used for the scf and nscf calculations of the supercell. The electronic structure was determined along the high symmetry path of Γ-X-M-Γ-Z-R-A-Z in the Brillouin zone.

3. Result and discussions

3.1 Crystal and microstructural analysis of tri-doped SnTe

In Fig. 1a, the XRD patterns of the synthesized samples were measured, and all main peaks were indexed to rock salt structure (JCPDS 46–1210, space group $Fm\bar{3}m$, No. 225). Peaks corresponding to Sn precipitates (JCPDS 04–0673) appeared after Mn doping exceeded 3% (in mole) ($SnMn_{0.03}Te$), and MnTe phase peaks (JCPDS 18–0814) were observed at the $SnMn_{0.10}Te$ sample (Fig. S1a). The formation of Sn precipitates results from the low formation energy of Sn vacancies (V''_{Sn}) [28]. This indicates that under Mn-rich doping conditions, Mn is well incorporated into Sn sites. After substituting Sn with Ge, the Sn precipitate peaks disappeared, and peaks corresponding to pure Ge precipitates (JCPDS 04–0545) emerged (Fig. S1b). Even with Bi doping, peaks indexed to pure Ge precipitates were still observed (Fig. 1a). Fig. 1b shows the enlarged diffraction peaks of the (024) planes from Fig. 1a, selected from the high-angle region for more reliable lattice parameter determination [66], and the calculated lattice parameters are summarized in Table S1. The smaller ionic radii of Mn^{2+} (0.66 Å) and Ge^{2+} (0.73 Å) compared to Sn^{2+} (0.93 Å), lead to a decrease in the lattice parameter [67]. When Bi is doped at the Sn site, the slightly larger ionic radius of Bi^{3+} (0.96 Å) substituting for Sn^{2+} (0.93 Å) increases the lattice parameter, with a slight peak shift to lower angles observed as the Bi doping content increases [67]. As a result, the lattice parameter tends to increase according to Vegard's law, indicating the well incorporation of Bi into SnTe under our experimental conditions at concentrations below 3% [55].

These analyses align with FE-EPMA quantitative results, and WDS point analysis data are summarized in Table 1. With increasing Mn doping content, the Mn atomic percent in the

matrix increases linearly, while the Sn atomic percent decreases, leading to Sn precipitation. As the Ge doping content increases, the Ge concentration in the SnTe matrix increases linearly. Bi doping up to 3% exhibits good solubility within the matrix phase. As shown in Fig. S2, the BSE images confirm the formation of dark, spherical nanoprecipitates along the grain boundaries of the gray matrix phase. According to the EDS line scanning results, Mn-rich phases were formed at the grain boundaries of the $SnMn_{0.06}Te$ sample, while peak signals of both Mn and Ge were detected at the grain boundaries of the $Sn_{0.90}Mn_{0.06}Ge_{0.10}Te$ and $Sn_{0.88}Mn_{0.06}Ge_{0.10}Bi_{0.02}Te$ samples.

To further investigate the microstructural features, FE-TEM was employed, and Fig. 2a presents the selected area electron diffraction (SAED) pattern along the $[\bar{1}00]$ zone axis, obtained from a single grain of the $Sn_{0.88}Mn_{0.06}Ge_{0.10}Bi_{0.02}Te$ sample. The diffraction spots were indexed as the rock salt structure of SnTe ($Fm\bar{3}m$), with interplanar distances of ~0.315 nm corresponding to the (002) plane. Additional weak diffraction spots were observed between the main diffraction spots (yellow circles). These additional spots were attributed to a coherently embedded nanostructure with short-range ordering, ~15 nm in size (white circle), observed in the high-resolution TEM (HRTEM) micrograph shown in Fig. 2b. In Fig. 2c, forbidden reflections of the rock salt structure at positions such as (001) and (021) were observed in the fast Fourier transform (FFT) performed on the embedded nanostructure within the red-boxed region in Fig. 2b. These forbidden reflections resulted from the doublet periodicity of the (002) planes in the embedded nanostructure. The schematic crystal structure and reciprocal lattice of the embedded nanostructure are shown in Fig. S4. These coherently embedded nanostructures should be a consequence of excess Mn doping in SnTe. Previous

studies on stoichiometric Mn doping have reported the formation of these nanostructures at doping contents above 12%, while they were not observed at lower doping contents (<7%) [47]. In the $Sn_{0.88}Mn_{0.06}Ge_{0.10}Bi_{0.02}Te$ sample, these coherently embedded nanostructures were densely distributed throughout the matrix, even at a Mn doping content of 6%. In addition to the embedded nanostructures in the matrix phase, precipitates were also observed along the grain boundaries (Fig. S2c). Fig. 2d shows an HRTEM image of one of the precipitates formed at the grain boundary, which has a diameter of approximately 30–50 nm. TEM-EDS mapping confirmed that these precipitates were Mn–Ge compounds (Fig. 2e), and the line scan result suggests that the composition of the precipitate is the Mn_2Ge compound (Fig. S5). Geometric phase analysis (GPA) was conducted on the region in Fig. 2f to examine the strain distribution in the SnTe matrix [68]. The GPA results, illustrated in Fig. 2g–i, represent the strain tensors ε_{xx}, ε_{yy}, and ε_{xy}, respectively. The analysis results show a deformation zone localized in the embedded nanostructures, with the matrix exhibiting a nearly uniform deformation distribution except around the Mn–Ge precipitates. Coherently embedded precipitates promote phonon scattering without significantly affecting carrier mobility, while the deformation around the Mn–Ge precipitates further enhances phonon scattering.

3.2 Electronic transport properties and band modification

Initially, SnTe was nonstoichiometrically doped with isovalent dopants Mn and Ge, and its electrical transport properties are presented in Fig. S6 and S7. Based on these results, the $Sn_{0.90}Mn_{0.06}Ge_{0.10}Te$ composition was selected for further improvement by introducing Bi as a don]or dopant. Since Bi ([Xe] $4f^{14}$ $5d^{10}$ $6s^2$ $6p^3$) exists as a Bi^{3+} at Sn^{2+} sites [55], it was

expected to successfully decrease the hole carrier concentration. In Fig. 3a, the temperature-dependent electrical conductivity of all samples exhibits degenerated semiconductor behavior, decreasing with increasing temperature. As the excess Mn content increases, the electrical conductivity decreases and drops from 8734 S/cm in pristine SnTe to 1289 S/cm in $SnMn_{0.10}Te$ at room temperature (Fig. S6a). The room temperature electrical conductivity increases to 3195 S/cm ($Sn_{0.90}Mn_{0.06}Ge_{0.10}Te$) with increasing Ge doping, while aliovalent Bi doping reduces it to 2356 S/cm ($Sn_{0.88}Mn_{0.06}Ge_{0.10}Bi_{0.02}Te$). Hall measurements at 298 K show that pristine SnTe exhibits a high hole carrier concentration of 3.10×10^{20} cm^{-3}, which decreases to 0.88×10^{20} cm^{-3} in the $SnMn_{0.06}Te$ sample (Fig. 3b). This reduction in carrier concentration is associated with a decrease in Sn vacancies, which is due to excess Mn doping. The Hall carrier concentration in the $Sn_{0.90}Mn_{0.06}Ge_{0.10}Te$ sample is 1.63×10^{20} cm^{-3}, while in the $Sn_{0.87}Mn_{0.06}Ge_{0.10}Bi_{0.03}Te$ sample, it is reduced to 0.99×10^{20} cm^{-3}. When Ge is substituted at Sn sites, the carrier concentration increases. Although Mn and Ge doping are generally known to increase the carrier concentration in SnTe [52,69], the samples presented in this study exhibit a lower carrier concentration compared to previous studies with similar compositions (Fig. 3c), demonstrating their effectiveness in optimizing carrier concentration. Compared to the $Sn_{0.82}Mn_{0.06}Ge_{0.10}Bi_{0.02}Te$ sample and the $Sn_{0.85}Mn_{0.06}Ge_{0.10}Bi_{0.02}Te$ sample, $Sn_{0.88}Mn_{0.06}Ge_{0.10}Bi_{0.02}Te$ sample shows a higher Hall mobility of 117 cm^2/Vs with a lower carrier concentration. These results indicate that coherently embedded nanostructures (Fig. 2c) provide effective carrier transport paths and reduce carrier scattering induced by ionized impurities and vacancies, thereby enhancing carrier mobility, unlike uniformly dispersed dopants in the matrix.

Fig. 3d illustrates the temperature-dependent Seebeck coefficient of the synthesized samples. The Seebeck coefficient is considerably enhanced after excess Mn doping, recording 70.2 μV/K at room temperature ($SnMn_{0.06}Te$). This value increases linearly with temperature, reaching 171.2 μV/K at 623 K and gradually approaching saturation at 191.4 μV/K at 823 K. The gradual saturation of the Seebeck coefficient above 623 K is associated with the bipolar effect [38]. When Ge is substituted at Sn sites, the Seebeck coefficient decreases to 38.3 μV/K in $Sn_{0.90}Mn_{0.06}Ge_{0.10}Te$ sample, primarily due to an increase in carrier concentration (Fig. 3b). However, beyond 623 K, the Seebeck coefficient increases linearly with temperature, reaching 175.4 μV/K at 873 K ($Sn_{0.90}Mn_{0.06}Ge_{0.10}Te$) and indicating suppressed bipolar effect. With increasing Bi doping contents, the Seebeck coefficient increased across all temperature ranges. In the $Sn_{0.88}Mn_{0.06}Ge_{0.10}Bi_{0.02}Te$ sample, the Seebeck coefficient increased within the measurement range without exhibiting a saturation trend, reaching its highest value of 202.8 μV/K at 873 K. Consequently, the $SnMn_{0.06}Te$ sample recorded a higher power factor than the other samples below 623 K (Fig. 3e). At higher temperatures, the suppression of the bipolar effect by Ge doping led to increased power factors in Ge-doped samples. Through the synergistic effect of Mn, Ge, and Bi doping, the $Sn_{0.88}Mn_{0.06}Ge_{0.10}Bi_{0.02}Te$ sample achieved a maximum power factor of 24.0 μW/(cm·K^2) at 873 K. Fig. 3f compares the proposed $Sn_{0.88}Mn_{0.06}Ge_{0.10}Bi_{0.02}Te$ sample with the $Sn_{0.82}Mn_{0.06}Ge_{0.10}Bi_{0.02}Te$ and the $Sn_{0.85}Mn_{0.06}Ge_{0.10}Bi_{0.02}Te$ sample. It also includes comparisons with other high-performance SnTe-based materials featuring similar compositions, such as Mn–Ge [52], Ge–Bi [70], Mn–Sb–Bi [38], Mn–Bi [44], Ge–Bi–Sb [39], and Bi–Cu–In [35]. In this comparison, the $Sn_{0.88}Mn_{0.06}Ge_{0.10}Bi_{0.02}Te$ sample recorded the peak power factor slightly lower than the ~25 μW/(cm·K^2) observed in Ge–Bi–Sb [39], Bi–Cu–In doped SnTe [35], and the

$Sn_{0.85}Mn_{0.06}Ge_{0.10}Bi_{0.02}Te$ sample. This slight difference originates from reduced electrical conductivity, leading to lower electronic thermal conductivity.

To understand the trend in the transport properties we studied the electronic structures of SnTe and the doped compositions. For the simulated supercell we find the principal band gap appearing at Γ point instead of L point and heavy carrier bands appearing at Z+δ in Z→R direction instead of Σ point due to folding of the Brillouin zone as reported previously [71,72]. The electronic structure of $Sn_{16}Te_{16}$ reveals a direct band gap of 0.081 eV (Fig. 4a). This underestimation of band gap is well known during DFT calculations [41]. The energy offset between the valence sub-bands is estimated to be 0.297 eV and that between the conduction sub-bands is estimated to be 0.241 eV. Hence, these heavy carrier bands do not contribute to transport properties making SnTe a poor thermoelectric material [73]. We observe in partial density of states (pDOS) plot that the conduction band has predominant contribution from the 'p' orbitals of Sn, while 'p' orbitals of Te along with 's' orbitals of Sn form the valence band (Fig. 4b). When we dope Mn in SnTe, we see a prominent increase in the band gap with a set of bands with width of 0.208 eV appearing 0.2 eV above the valence band maximum (Fig. 4c). This set of bands has major contribution from the 'd' orbitals of Mn (Fig. 4d). The energy offset between the light hole valence band at Γ point and heavy hole valence band at Z+δ in Z→R direction decreases to 0.075 eV. Such drastic convergence leads to increase in Nv from 4 (fro m light hole valence sub-bands) to 16 (4 from light hole valence sub-bands and 12 from heav y hole valence sub-bands) while increase in DOS at the Fermi level increases the band effective mass m_b^* [74]. Both these lead to increase in the DOS effective mass, m^* and in turn Seebeck values as observed experimentally [72]. Further doping of Ge leads to decrease in the width of

the flat bands introduced by the ‘d’ orbitals of Mn to 0.194 eV and hence increase in the band gap leading to suppression of the bipolar effect which is also observed experimentally (Fig. 5a and b). The energy offset between the valence sub-bands increases to 0.136 eV leading to decrease in the DOS effective mass which is also observed experimentally. Further doping of Bi leads to introduction of resonance states as previously reported with decrease in the band gap (Fig. 5c and d) [53,54]. We also observe that decrease in the DOS effective mass is due to the Ge doping as in the multi-doped composition as number of Ge atoms increase from 1 (Fig. S9) to 2 (Fig. 5c) the valence band offset increases from 0.199 eV to 0.225 eV. The resonance states formed due to ‘p’ orbitals of Bi is seen to cap the valence band edge in both the conf igurations. As the resonance states formed due to hybridization of ‘p’ orbitals of the dopant li ke Bi is quite broader and less intense than those formed due to ‘s’ orbitals of the dopants like In or Zn, here we see the effect of ‘p’ orbitals of Bi in the range of 0 to 0.5 eV (compare, Fig 5 b and Fig 5d) [53,54,75]. At the Fermi level and slightly below it the intense DOS resulting d ue to ‘d’ orbitals of Mn overpowers the contribution from ‘p’ orbitals of bismuth. These simulation results were further supported by experimental measurements, as shown in Fig. S10. In Fig. S10a, a Pisarenko plot was constructed to analyze the effect of each dopant on the effective mass, with a theoretical prediction line based on the valence band model (VBM) applied [29,76]. In Fig. S10b, FT-IR transmittance measurements were conducted to investigate the band gap variations induced by each dopant in SnTe [77]. Based on both experimental and theoretical results, it was confirmed that, under our synthesis conditions, Mn was the most effective dopant for increasing the effective mass and promoting band structure convergence, while Ge mainly contributed to further band gap widening. The effect of Bi doping on the band gap was not clearly observed in the Tauc plot, and the increase in the Seebeck coefficient upon

Bi doping is attributed to a reduction in carrier concentration.

3.3 Thermal transport properties

The pristine SnTe sample exhibits intrinsically high thermal conductivity [78]. This characteristic primarily arises from its high electronic thermal conductivity [78]. In all samples, the reduced carrier concentration diminishes the contribution of electronic thermal conductivity, leading to a significant decrease in total thermal conductivity, in Fig. 6a. The decrease in total thermal conductivity resulting from Bi doping is mainly caused by a notable reduction in electronic thermal conductivity, as illustrated in Fig. 6b. At lower temperatures, the lattice thermal conductivity of $Sn_{0.90-z}Mn_{0.06}Ge_{0.10}Bi_zTe$ samples decreases with increasing Bi content (Fig. 6c). However, at 873K, the $Sn_{0.89}Mn_{0.06}Ge_{0.10}Bi_{0.01}Te$ sample exhibits the lowest lattice thermal conductivity of 0.721 W/(m·K), while the lattice thermal conductivity increases with Bi doping content, reaching 0.899 W/(m·K) for the $Sn_{0.87}Mn_{0.06}Ge_{0.10}Bi_{0.03}Te$ sample. Plotting the lattice thermal conductivity as a function of the reciprocal of temperature allows for the separation of lattice thermal conductivity contributions from other factors, as shown in Fig. 6d [79]. The $SnMn_{0.06}Te$ sample exhibits a linear decreasing trend at low temperatures but begins to saturate above 523 K, suggesting the onset of the bipolar effect. For the $Sn_{0.88}Mn_{0.06}Ge_{0.10}Bi_{0.02}Te$ sample, the lattice thermal conductivity decreases linearly up to 773 K as a result of the increased band gap and higher carrier concentration. The $Sn_{0.82}Mn_{0.06}Ge_{0.10}Bi_{0.02}Te$ sample was compared with the $Sn_{0.88}Mn_{0.06}Ge_{0.10}Bi_{0.02}Te$ sample. In the $Sn_{0.88}Mn_{0.06}Ge_{0.10}Bi_{0.02}Te$ sample, the lattice thermal conductivity significantly decreases in the low-temperature region, with Mn-Ge precipitates along the grain boundaries and the

embedded nanostructures causing deformation in the matrix, thereby contributing as phonon scattering sites.

To further understand the lattice thermal conductivity, we analyzed the spectral lattice thermal conductivity using the Debye–Callaway model (Fig. 7a) [79]. Details of the calculation method are provided in the Supplementary material. In the low- to mid-frequency range, phonon scattering was primarily governed by grain boundaries and Mn–Ge nanoprecipitates. At higher frequencies, point defect scattering became dominant, with Mn dopant contributing the most and Bi dopant the least. Although Bi has a large atomic mass difference from Sn, its minimal ionic radius mismatch and low doping concentration limited its contribution to phonon scattering in the Debye–Callaway model. Raman spectroscopy was performed to investigate the effect of each dopant on the lattice thermal conductivity, as shown in Fig. 7b. The results revealed peaks corresponding to the longitudinal optical phonon modes (A_1) at 124 cm^{-1} and the transverse optical phonon modes (E_{TO}) at 142 cm^{-1} in pristine SnTe, consistent with previous reports [80,81]. In the excess Mn doped sample ($SnMn_{0.06}Te$), the peaks shifted to lower frequencies compared to the pristine sample, while the Ge-doped sample ($Sn_{0.90}Mn_{0.06}Ge_{0.10}Te$) exhibited no significant changes. In the $Sn_{0.88}Mn_{0.06}Ge_{0.10}Bi_{0.02}Te$ sample, a significant redshift was observed, with A_1 at 119 cm^{-1} and E_{TO} at 139 cm^{-1}, indicating a weakening of bonding strength, which can lead to lattice softening and reduced sound velocity [27,35]. This behavior is explained by the relationship $f \sim (K/\mu)^{0.5}$, where f is the phonon frequency, K is the force constant of a bond, and μ is the reduced mass [80,82]. Lattice softening caused by Bi doping, which reduced sound velocity [35,59], was the primary factor lowering the lattice thermal conductivity.

3.4 Figure of Merit *zT* and Output Performance

The maximum *zT* value of ~1.32 at 873 K was achieved in the $Sn_{0.88}Mn_{0.06}Ge_{0.10}Bi_{0.02}Te$ sample, as shown in Fig. 8a. Below 573 K, the $SnMn_{0.06}Te$ sample exhibited a higher *zT* than the other samples, achieving a tenfold increase (~0.01) over the pristine SnTe sample (~0.001) at room temperature. This improvement in *zT* is attributed to excess Mn doping in SnTe, which enhanced the Seebeck coefficient through the formation of a resonance states and band convergence. Above 573 K, the tri-doping method significantly increased *zT*. Ge doping in SnTe expanded the band gap, suppressing the bipolar effect, while Bi doping reduced sound velocity and optimized carrier concentration. In Fig. 8b, the thermoelectric performance of the synthesized samples in this study was compared to that of other high-performance SnTe-based materials with similar compositions to our samples [35,38,39,44,52,70]. Although the $Sn_{0.88}Mn_{0.06}Ge_{0.10}Bi_{0.02}Te$ sample had a slightly lower power factor than Ge–Bi–Sb [39], Bi–Cu–In doped SnTe [35], and $Sn_{0.85}Mn_{0.06}Ge_{0.10}Bi_{0.02}Te$ (Fig. 3f), it achieved the highest *zT* by reducing electronic thermal conductivity through optimized carrier concentration. In addition, the formation of nanoprecipitates through grain boundary engineering and nanostructuring effectively scattered mid-frequency phonons, significantly reducing thermal conductivity from low to mid temperatures. As a result, the $Sn_{0.88}Mn_{0.06}Ge_{0.10}Bi_{0.02}Te$ sample achieved an improved average *zT* of ~0.53, which is higher than the ~0.44 observed for the $Sn_{0.82}Mn_{0.06}Ge_{0.10}Bi_{0.02}Te$ sample.

To investigate the energy conversion efficiency of the fabricated thermoelectric materials, we measured the output voltage, current, and power from a heterogeneous two-pair

leg-based TEG (Fig. S11a), consisting of a p-type $Sn_{0.88}Mn_{0.06}Ge_{0.10}Bi_{0.02}Te$ block and an n-type $Pb_{0.92}Bi_{0.08}Te$ block (Fig. S12), under various temperature gradients (ΔT) using a home-built measurement system (Fig. S11b) [83]. The p-type and n-type legs exhibit less than 5% difference in thermal expansion coefficients (CTE) across the temperature range (Fig. S13), indicating good CTE compatibility. As shown in the voltage-current-power curves of Fig. 9, the fabricated TEG converted a maximum output power of 661 μW at ΔT = 485 K (T_{hot} = 773 K). Previous studies on SnTe-based TEGs have explored single-leg TEGs [84,85] simulations [86], and Bi_2Te_3-based n-type materials [37,87]. In this study, we employed PbTe as the n-type material, allowing measurements up to 773 K. Despite the comparable thermal and electrical transport properties of SnTe and PbTe (Fig. S12), the measured output power was lower than the simulated value of ~1400 μW at ΔT = 300 K. The simulation result is shown in Fig. S14. This discrepancy is mainly due to oxidation-induced degradation in PbTe, as shown in Fig. S15. For the practical commercialization of thermoelectric generators, further research on oxidation-resistant barrier layers for mid-temperature operation is required. This work further expands upon existing research, proposing a novel approach for mid-temperature thermoelectric applications.

4. Conclusions

In summary, we have successfully introduced grain boundary engineering and nanostructuring in SnTe. This was achieved through tri-doping of Mn, Ge, and Bi in the nonstoichiometrically synthesized SnTe. Mn–Ge precipitates and coherently embedded nanostructures effectively scattered mid-frequency phonons, reducing lattice thermal

conductivity. The tri-doping of Mn, Ge, and Bi synergistically modified the band structure, while reducing the carrier concentration without compromising Hall mobility. As a result of the unique microstructures and the synergistic effect of each dopant, the $Sn_{0.88}Mn_{0.06}Ge_{0.10}Bi_{0.02}Te$ sample achieved a high zT of 1.32 at 873K, which is higher than that of previously reported samples with similar compositions. Additionally, compared to conventionally tri-doped samples, the zT_{max} increased by about 23%, and the zT_{avg} increased by approximately 20%. This study highlights the grain boundary engineering and nanostructuring through the tri-doping of Mn, Ge, and Bi as an effective strategy for enhancing the thermoelectric performance of SnTe-based materials.

Acknowledgements

This work was supported by grants from the National Research Foundation (NRF) of Korea, and funded by the Korean government (MSIT) (RS-2025-02223651). This study was supported by the BK21 Four project funded by the Ministry of Education, Korea (2120231314753). The author (USS) acknowledges the grant from Science and Engineering Research Board, Department of Science and Technology, Government of India under SERB Research Scientist scheme.

Declaration of Interest Statement

The authors declare that they have no known competing financial interests or personal relationships that could have appeared to influence the work reported in this paper.

References

[1] Shi X-L, Zou J, Chen Z-G. Advanced thermoelectric design: From materials and structures to devices. Chem Rev 2020;120:7399–7515.

[2] Tan G, Zhao L-D, Kanatzidis MG. Rationally designing high-performance bulk thermoelectric materials. Chem Rev 2016;116:12123–12149.

[3] Sun F-H, Li H, Tan J, Zhao L, Wang X, Hu H, et al. Review of current $zT > 1$ thermoelectric sulfides. J Materiomics 2024;10:218–233.

[4] Amirkhizi P, Hedayati M, Madre MA, Dura OJ, Torres MA, Sotelo A, et al. Fabrication and testing of ceramic thermoelectric multi-leg module for high-temperature energy conversion. J Alloys Compd 2025;1013:178628.

[5] Jung C, Jang K, Park H, Jang J, Jang H, Kang B, et al. Enhanced thermoelectric properties of NbCoSn half-Heuslers through *in-situ* nanocrystallization of amorphous precursors during the consolidation process. J Mater Sci Technol 2023;165:39–48.

[6] Zhang X, Zhao LD. Thermoelectric materials: Energy conversion between heat and electricity. J Materiomics 2015;1:92–105.

[7] Wang G, Yang J, Zhao H. $Mg_3(Bi, Sb)_2$-based thermoelectric modules towards near-room temperature cooling and power generation. J Materiomics 2022;8:1218–1221.

[8] Niu X, Yu J, Wang S. Experimental study on low-temperature waste heat thermoelectric generator. J Power Sources 2009;188:621–626.

[9] Wei T-R, Wu C-F, Li F, Li J-F. Low-cost and environmentally benign selenides as

promising thermoelectric materials. J Materiomics 2018;4:304–320.

[10] Feng H, Deng Q, Zhong Y, Rao X, Wang Y, Zhu J, et al. Annealing engineering induced high thermoelectric performance in Yb-filled $CoSb_3$ skutterudites. J Mater Sci Technol 2023;150:168–174.

[11] Pan H, Sun Z, Geng H, Chang Q, Zhang B, Zhang L. Thermal stability optimization of single-leg skutterudite-based thermoelectric devices based on lattice distortion effects. J Materiomics 2024;11:100859.

[12] Graf T, Felser C, Parkin SSP. Simple rules for the understanding of Heusler compounds. Prog Solid State Chem 2011;39:1–50.

[13] Kahiu JN, Kihoi SK, Kim H, Lee HS. Thermoelectric and Magnetic Properties of Biphasic $ZrFe_{0.5}Ni_{0.5}Sb$ Double Half-Heusler and ZrNiSb Half-Heusler Induced by Co Doping. ACS Appl Electron Mater 2024;6:1829–1840.

[14] Yin S, Li Q, Wang S, Chen J, Dong Z, Zhang Y, et al. Structure and thermoelectric properties of half-Heusler-like TiFeCuSb alloys. J Materiomics 2024;10:523–530.

[15] Zhao L-D, Lo S-H, Zhang Y, Sun H, Tan G, Uher C, et al. Ultralow thermal conductivity and high thermoelectric figure of merit in SnSe crystals. Nature 2014;508:373–377.

[16] Kim H, Kihoi SK, Lee HS. Point defects control in non-stoichiometric $CuInTe_2$ compounds and its corresponding effects on the microstructure and thermoelectric properties. J Alloys Compd 2021;869:159381.

[17] Heremans JP, Jovovic V, Toberer ES, Saramat A, Kurosaki K, Charoenphakdee A, et al.

Enhancement of Thermoelectric Efficiency in PbTe by Distortion of the Electronic Density of States. Science 2008;321:554–557.

[18] Kim H, Kihoi SK, Shenoy US, Kahiu JN, Shin DH, Bhat DK, et al. High thermoelectric and mechanical performance achieved by a hyperconverged electronic structure and low lattice thermal conductivity in GeTe through $CuInTe_2$ alloying. J Mater Chem A 2023;11:8119–30.

[19] Min Y, Roh JW, Yang H, Park M, Kim S Il, Hwang S, et al. Surfactant-Free Scalable Synthesis of Bi_2Te_3 and Bi_2Se_3 Nanoflakes and Enhanced Thermoelectric Properties of Their Nanocomposites. Adv Mater 2013;25:1425–1429.

[20] Chen Y, Wu H, Han G, Zhang B, Lu X, Yang W, et al. Synergistic effects lead to high thermoelectric performance of iodine doped pseudo-binary layered $GeSb_2Te_4$. J Materiomics 2025;11:100973.

[21] Parida A, Naik R. Advances in metal telluride thin films: A comprehensive review of properties and emerging applications. J Alloys Compd 2025;1010:177519.

[22] Han C, Sun Q, Li Z, Dou SX. Thermoelectric enhancement of different kinds of metal chalcogenides. Adv Energy Mater 2016;6:1600498.

[23] Shi Y, Sturm C, Kleinke H. Chalcogenides as thermoelectric materials. J Solid State Chem 2019;270:273–279.

[24] Wang Y, Yuan Y, Yang R, Li M, Liu T, Tahashi M, et al. High thermoelectric performance of SnTe–MnSe with low lattice thermal conductivity. ACS Appl Energy Mater 2024;7:145–153.

[25] Kihoi SK, Yang T, Lee HS. Recent progress in SnTe: An eco-friendly and high-performance chalcogenide thermoelectric material. Small 2025; 21(4): 2409315.

[26] Peng P-P, Wang C, Li L-W, Li S-Y, Chen Y-Q. Research status and performance optimization of medium-temperature thermoelectric material SnTe. Chinese Phys B 2022;31:047307.

[27] Chen Z, Guo X, Zhang F, Shi Q, Tang M, Ang R. Routes for advancing SnTe thermoelectrics. J Mater Chem A 2020;8:16790–16813.

[28] Wang N, West D, Liu J, Li J, Yan Q, Gu B-L, et al. Microscopic origin of the p-type conductivity of the topological crystalline insulator SnTe and the effect of Pb alloying. Phys Rev B 2014;89:045142.

[29] Zhang Y, Sun J, Shuai J, Tang X, Tan G. Lead-free SnTe-based compounds as advanced thermoelectrics. Mater Today Phys 2021;19:100405.

[30] Dimmock JO, Melngailis I, Strauss AJ. BAND STRUCTURE AND LASER ACTION IN $Pb_xSn_{1-x}Te$. Phys Rev Lett 1966;16:1193–1196.

[31] Su D, Cheng J, Li S, Zhang S, Lyu T, Zhang C, et al. Inhibiting the bipolar effect *via* band gap engineering to improve the thermoelectric performance in n-type $Bi_{2-x}Sb_xTe_3$ for solid-state refrigeration. J Mater Sci Technol 2023;138:50–58.

[32] Chen Z, Li J, Tang J, Zhang F, Zhong Y, Liu H, et al. Boosting thermoelectrics by alloying Cu_2Se in SnTe-CdTe compounds. J Mater Sci Technol 2021;89:45–51.

[33] Tan G, Zhao L-D, Shi F, Doak JW, Lo S-H, Sun H, et al. High thermoelectric

performance of p-type SnTe *via* a synergistic band engineering and nanostructuring approach. J Am Chem Soc 2014;136:7006–7017.

[34] Hussain T, Li X, Danish MH, Rehman MU, Zhang J, Li D, et al. Realizing high thermoelectric performance in eco-friendly SnTe *via* synergistic resonance levels, band convergence and endotaxial nanostructuring with Cu_2Te. Nano Energy 2020;73:104832.

[35] Kihoi SK, Shenoy US, Kim H, Kahiu JN, Kim CM, Park K, et al. Enhanced Electrical, Thermal, and Mechanical Properties of SnTe through Equimolar Multication Alloying for Suitable Device Applications. ACS Appl Energy Mater 2024;7:1149–1161.

[36] Xu J, Zhou Z, Zhang K, Zhao T, Wei Y, Zhang B, et al. Band and microstructure engineering toward high thermoelectric performance in SnTe. J Mater Chem A 2024;12:21790–21798.

[37] Zhang Q, Wang R, Song K, Tan X, Hu H, Guo Z, et al. Raised solubility in SnTe by $GeMnTe_2$ alloying enables converged valence bands, low thermal conductivity, and high thermoelectric performance. Nano Energy 2022;94:106940.

[38] Kihoi SK, Kim H, Jeong H, Kim H, Ryu J, Yi S, et al. Thermoelectric properties of Mn, Bi, and Sb co-doped SnTe with a low lattice thermal conductivity. J Alloys Compd 2019;806:361–369.

[39] Kihoi SK, Shenoy US, Kahiu JN, Kim H, Bhat DK, Lee HS. Pushing the limit of synergy in SnTe-based thermoelectric materials leading to an ultra-low lattice thermal conductivity and enhanced ZT. Sustain Energy Fuels 2023;7:1916–1929.

[40] Tan X, Liu G, Xu J, Tan X, Shao H, Hu H, et al. Thermoelectric properties of In-Hg co-

doping in SnTe: Energy band engineering. J Materiomics 2018;4:62–67.

[41] Bhat DK, Shenoy US. Zn: A versatile resonant dopant for SnTe thermoelectrics. Mater Today Phys 2019;11:100158.

[42] Bhat DK, Shenoy US. Enhanced thermoelectric performance of bulk tin telluride: Synergistic effect of calcium and indium co-doping. Mater Today Phys 2018;4:12–18.

[43] Banik A, Shenoy US, Anand S, Waghmare U V., Biswas K. Mg Alloying in SnTe Facilitates Valence Band Convergence and Optimizes Thermoelectric Properties. Chem Mater 2015;27:581–587.

[44] Kihoi SK, Kahiu JN, Kim H, Shenoy US, Bhat DK, Yi S, et al. Optimized Mn and Bi co-doping in SnTe based thermoelectric material: A case of band engineering and density of states tuning. J Mater Sci Technol 2021;85:76–86.

[45] Zhang F, Li R, Gan L, Tan X, He S, Tian B, et al. Lattice modulation and electronic band optimization in Q-doped SnTe-GeTe alloys (Q = Bi, Sb, and Ag). Sci China Mater 2023;66:3659–69.

[46] Li W, Chen Z, Lin S, Chang Y, Ge B, Chen Y, et al. Band and scattering tuning for high performance thermoelectric $Sn_{1-x}Mn_xTe$ alloys. J Materiomics 2015;1:307–315.

[47] Tan G, Shi F, Hao S, Chi H, Bailey TP, Zhao L-D, et al. Valence band modification and high thermoelectric performance in SnTe heavily alloyed with MnTe. J Am Chem Soc 2015;137:11507–11516.

[48] Wu H, Chang C, Feng D, Xiao Y, Zhang X, Pei Y, et al. Synergistically optimized

electrical and thermal transport properties of SnTe *via* alloying high-solubility MnTe. Energy Environ Sci 2015;8:3298–3312.

[49] Banik A, Ghosh T, Arora R, Dutta M, Pandey J, Acharya S, et al. Engineering ferroelectric instability to achieve ultralow thermal conductivity and high thermoelectric performance in $Sn_{1-x}Ge_xTe$. Energy Environ Sci 2019;12:589–595.

[50] Tang J, Gao B, Lin S, Li J, Chen Z, Xiong F, et al. Manipulation of Band Structure and Interstitial Defects for Improving Thermoelectric SnTe. Adv Funct Mater 2018;28:1–7.

[51] Yang H, Wu L, Feng X, Wang H, Huang X, Duan B, et al. Optimization of mechanical and thermoelectric properties of SnTe-based semiconductors by mn alloying modulated precipitation evolution. Small 2024;20.

[52] Li JQ, Huang S, Chen ZP, Li Y, Song SH, Liu FS, et al. Phases and thermoelectric properties of SnTe with (Ge, Mn) co-doping. Phys Chem Chem Phys 2017;19:28749–28755.

[53] Shenoy US, Bhat DK. Improving the *zT* of SnTe using electronic structure engineering: Unusual behavior of Bi dopant in the presence of Pb as a co-dopant. Mater Adv 2021;2:6267–6271.

[54] Shenoy US, Bhat DK. Electronic structure engineering of tin telluride through co-doping of bismuth and indium for high performance thermoelectrics: A synergistic effect leading to a record high room temperature *zT* in tin telluride. J Mater Chem C 2019;7:4817–4821.

[55] Zhou Z, Yang J, Jiang Q, Luo Y, Zhang D, Ren Y, et al. Multiple effects of Bi doping

in enhancing the thermoelectric properties of SnTe. J Mater Chem A 2016;4:13171–13175.

[56] Li K, Sun L, Bai W, Ma N, Zhao C, Zhao J, et al. High-entropy strategy to achieve electronic band convergence for high-performance thermoelectrics. J Am Chem Soc 2024;146:14318–14327.

[57] Hu L, Zhang Y, Wu H, Li J, Li Y, Mckenna M, et al. Entropy engineering of SnTe: Multi-principal-element alloying leading to ultralow lattice thermal conductivity and state-of-the-art thermoelectric performance. Adv Energy Mater 2018;8:1802116.

[58] Guo F, Cui B, Liu Y, Meng X, Cao J, Zhang Y, et al. Thermoelectric SnTe with band convergence, dense dislocations, and interstitials through Sn self-compensation and Mn alloying. Small 2018;14:1–10.

[59] Kihoi SK, Shenoy US, Bhat DK, Lee HS. Complementary effect of co-doping aliovalent elements Bi and Sb in self-compensated SnTe-based thermoelectric materials. J Mater Chem C 2021;9:9922–9931.

[60] Tauc J. Optical properties and electronic structure of amorphous Ge and Si. Mater Res Bull 1968;3:37–46.

[61] Makuła P, Pacia M, Macyk W. How to correctly determine the band gap energy of modified semiconductor photocatalysts based on UV–Vis spectra. J Phys Chem Lett 2018;9:6814–6817.

[62] Coulter JB, Birnie DP. Assessing tauc plot slope quantification: ZnO thin films as a model system. Phys Status Solidi 2018;255:1–7.

[63] Kim HS, Gibbs ZM, Tang Y, Wang H, Snyder GJ. Characterization of Lorenz number with Seebeck coefficient measurement. APL Mater 2015;3:041506.

[64] Giannozzi P, Baroni S, Bonini N, Calandra M, Car R, Cavazzoni C, et al. QUANTUM ESPRESSO: a modular and open-source software project for quantum simulations of materials. J Phys Condens Matter 2009;21:395502.

[65] Perdew JP, Burke K, Ernzerhof M. Generalized gradient approximation made simple. Phys Rev Lett 1996;77:3865–3868.

[66] King HW, Payzant EA. Error corrections for X-RAY powder diffractometry. Can Metall Q 2001;40:385–394.

[67] Shannon RD. Revised effective ionic radii and systematic studies of interatomic distances in halides and chalcogenides. Acta Crystallogr Sect A 1976;32:751–767.

[68] Hÿtch MJ, Snoeck E, Kilaas R. Quantitative measurement of displacement and strain fields from HREM micrographs. Ultramicroscopy 1998;74:131–146.

[69] He J, Tan X, Xu J, Liu G-Q, Shao H, Fu Y, et al. Valence band engineering and thermoelectric performance optimization in SnTe by Mn-alloying *via* a zone-melting method. J Mater Chem A 2015;3:19974–9.

[70] Nie C, Wang C, Xu Y, Liu Y, Niu X, Li S, et al. Band modification and localized lattice engineering leads to high thermoelectric performance in Ge and Bi codoped SnTe–$AgBiTe_2$ alloys. Small 2023;19:1–9.

[71] Shenoy US, Bhat DK. Molybdenum as a versatile dopant in SnTe: A promising material

for thermoelectric application. Energy Adv 2022;1:9–14.

[72] Shenoy US, Bhat DK. Vanadium: A Protean Dopant in SnTe for Augmenting Its Thermoelectric Performance. ACS Sustain Chem Eng 2021;9:13033–13038.

[73] Shenoy US, Bhat DK. Towards achieving an ideal convergence of light and heavy electron conduction bands in SnTe: Insights into copper doping. J Alloy Compd Commun 2024;1:100001.

[74] Shenoy US, D. GK, Bhat DK. A case of perfect convergence of light and heavy hole valence bands in SnTe: the role of Ge and Zn co-dopants. Mater Adv 2022;3:5941–5946.

[75] Bhat DK, Shenoy US. SnTe thermoelectrics: Dual step approach for enhanced performance. J Alloys Compd 2020;834:155181.

[76] Kihoi SK, Shenoy US, Kahiu JN, Kim H, Bhat DK, Lee HS. Ultralow lattice thermal conductivity and enhanced mechanical properties of Cu and Sb co-doped SnTe thermoelectric material with a complex microstructure evolution. ACS Sustain Chem Eng 2022;10:1367–1372.

[77] Makuła P, Pacia M, Macyk W. How to correctly determine the band gap energy of modified semiconductor photocatalysts based on UV-Vis spectra. J Phys Chem Lett 2018;9:6814–6817.

[78] Moshwan R, Yang L, Zou J, Chen Z. Eco-friendly SnTe thermoelectric materials: Progress and future challenges. Adv Funct Mater 2017;27:30–44.

[79] Chen Z, Zhang X, Pei Y. Manipulation of phonon transport in thermoelectrics. Adv

Mater 2018;30:1–12.

[80] Xie G, Li Z, Luo T, Bai H, Sun J, Xiao Y, et al. Band inversion induced multiple electronic valleys for high thermoelectric performance of SnTe with strong lattice softening. Nano Energy 2020;69:104395.

[81] Wang H, Hwang J, Zhang C, Wang T, Su W, Kim H, et al. Enhancement of the thermoelectric performance of bulk SnTe alloys *via* the synergistic effect of band structure modification and chemical bond softening. J Mater Chem A 2017;5:14165–14173.

[82] Badger RM. A relation between internuclear distances and bond force constants. J Chem Phys 1934;2:128–131.

[83] Park JM, Hyeon DY, Ma H-S, Kim S, Kim S-T, Nguyen YN, et al. Enhanced output power of thermoelectric modules with reduced contact resistance by adopting the optimized Ni diffusion barrier layer. J Alloys Compd 2021;884:161119.

[84] An D, Wang J, Zhang J, Zhai X, Kang Z, Fan W, et al. Retarding Ostwald ripening through Gibbs adsorption and interfacial complexions leads to high-performance SnTe thermoelectrics. Energy Environ Sci 2021;14:5469–5479.

[85] Wang T, Dou K, Wang H, Kim J, Wang X, Su W, et al. Higher-order anharmonicity leads to ultra-low thermal conductivity and high output power density of SnTe-based thermoelectric materials and modules. Mater Today Phys 2022;26:100748.

[86] Wang X, Wang H, Su W, Zhai J, Wang T, Chen T, et al. Optimization of the performance of the SnTe uni-leg thermoelectric module *via* metallized layers. Renew Energy

2019;131:606–616.

[87] Zhang Q, Guo Z, Wang R, Tan X, Song K, Sun P, et al. High-performance thermoelectric material and module driven by medium-entropy engineering in SnTe. Adv Funct Mater 2022;32.

Figure

Fig. 1. (a) XRD patterns of $Sn_{0.90-z}Mn_{0.06}Ge_{0.10}Bi_zTe$ samples, (b) enlarged diffraction peaks corresponding to the (024) planes in (a).

Fig. 2. (a) SAED pattern along the [$\bar{1}$**00**] zone axis from a single grain of the $Sn_{0.88}Mn_{0.06}Ge_{0.10}Bi_{0.02}Te$ sample and (b) corresponding HRTEM micrograph showing embedded nanostructures within the grain. (c) FFT image of the embedded nanostructure, (d) HRTEM micrograph showing nanoprecipitate along the grain boundary. (e) HAADF image with corresponding EDS elemental mapping of Sn, Te, Mn, Ge, and Bi. (f) HRTEM micrograph with GPA mappings: (g) ε_{xx}, (h) ε_{yy}, and (i) ε_{xy}.

Fig. 3. (a) Temperature-dependent electrical conductivity, (b) Hall measurement data at room temperature of $Sn_{0.90-z}Mn_{0.06}Ge_{0.10}Bi_zTe$ samples. (c) Hall mobility as a function of carrier concentration compared with previously reported data. Temperature-dependent (d) Seebeck coefficient, and (e) power factor of of $Sn_{0.90-z}Mn_{0.06}Ge_{0.10}Bi_zTe$ samples. (f) comparison of the maximum power factor obtained in this work with other high-performance SnTe-based materials.

Fig. 4. Electronic structure and pDOS of (a–b) $Sn_{16}Te_{16}$, (c–d) $Sn_{15}MnTe_{16}$. Energies are shifted with respect to Fermi level which is set to zero.

Fig. 5. Electronic structure and pDOS of (a–b) $Sn_{13}MnGe_2Te_{16}$, (c–d) $Sn_{12}MnGe_2BiTe_{16}$. Energies are shifted with respect to Fermi level which is set to zero.

Fig. 6. Temperature-dependent (a) total thermal conductivity, (b) electronic thermal conductivity, and (c) lattice thermal conductivity of synthesized $Sn_{0.90-z}Mn_{0.06}Ge_{0.10}Bi_zTe$ samples, and (d) lattice thermal conductivity plotted against the reciprocal of temperature for representative samples.

Fig. 7. (a) Spectral lattice thermal conductivity calculated as a function of phonon frequency based on various phonon scattering processes. (b) Raman spectroscopy results of representative samples.

Fig. 8. (a) Temperature-dependent zT of $Sn_{0.90-z}Mn_{0.06}Ge_{0.10}Bi_zTe$ samples. (b) Comparison of maximum and average zT values of the synthesized samples with previously reported SnTe-based compounds.

Fig. 9. Voltage-current-power curves measured from the $Sn_{0.88}Mn_{0.06}Ge_{0.10}Bi_{0.02}Te$-based two-pair TEG under various ΔT.

Table 1 EPMA analyzed composition of the matrix of the samples.

Sample	**EPMA analyzed composition (%, in mole)**
$SnMn_{0.05}Te$	$Sn_{49.10}Mn_{2.29}Te_{48.61}$
$SnMn_{0.06}Te$	$Sn_{48.91}Mn_{3.64}Te_{47.45}$
$SnMn_{0.07}Te$	$Sn_{47.09}Mn_{4.36}Te_{48.55}$
$SnMn_{0.10}Te$	$Sn_{46.30}Mn_{5.13}Te_{48.57}$
$Sn_{0.95}Mn_{0.06}Ge_{0.05}Te$	$Sn_{46.72}Mn_{2.41}Ge_{1.34}Te_{49.53}$
$Sn_{0.90}Mn_{0.06}Ge_{0.10}Te$	$Sn_{44.26}Mn_{3.47}Ge_{2.45}Te_{49.82}$
$Sn_{0.85}Mn_{0.06}Ge_{0.15}Te$	$Sn_{43.59}Mn_{3.48}Ge_{3.94}Te_{48.99}$
$Sn_{0.89}Mn_{0.06}Ge_{0.10}Bi_{0.01}Te$	$Sn_{44.73}Mn_{3.11}Ge_{1.86}Bi_{0.52}Te_{49.78}$
$Sn_{0.88}Mn_{0.06}Ge_{0.10}Bi_{0.02}Te$	$Sn_{44.44}Mn_{2.87}Ge_{2.07}Bi_{1.05}Te_{49.57}$
$Sn_{0.87}Mn_{0.06}Ge_{0.10}Bi_{0.03}Te$	$Sn_{43.95}Mn_{3.13}Ge_{2.00}Bi_{1.53}Te_{49.39}$

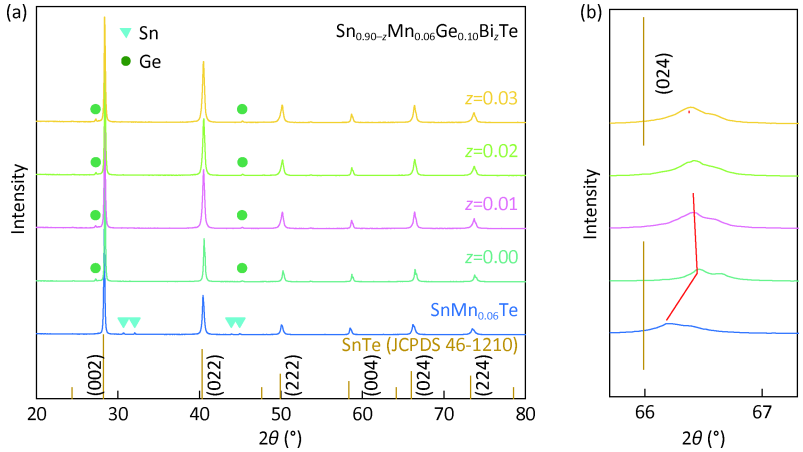

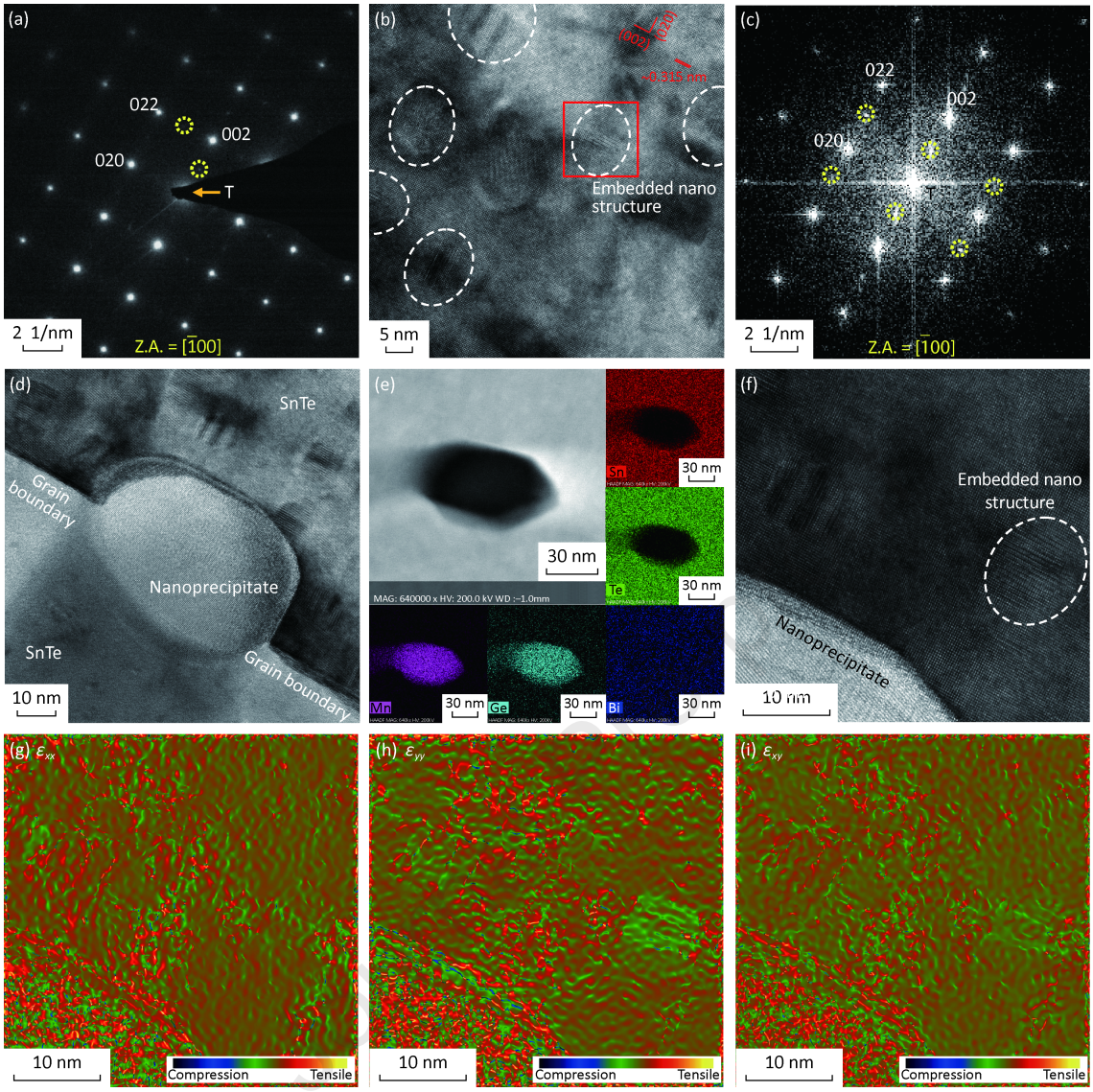
(a)
022
002
020
T
2 1/nm
Z.A. = [1̄00]
(b)
(002)
0.315 nm
Embedded nano structure
5 nm
(c)
022
002
020
T
2 1/nm
Z.A. = [1̄00]
(d)
SnTe
Grain boundary
Nanoprecipitate
SnTe
Grain boundary
10 nm
(e)
30 nm
Sn
Te
Mn
Ge
Bi
(f)
Embedded nano structure
Nanoprecipitate
10 nm
(g) ε_{xx}
(h) ε_{yy}
(i) ε_{xy}
10 nm
Compression
Tensile

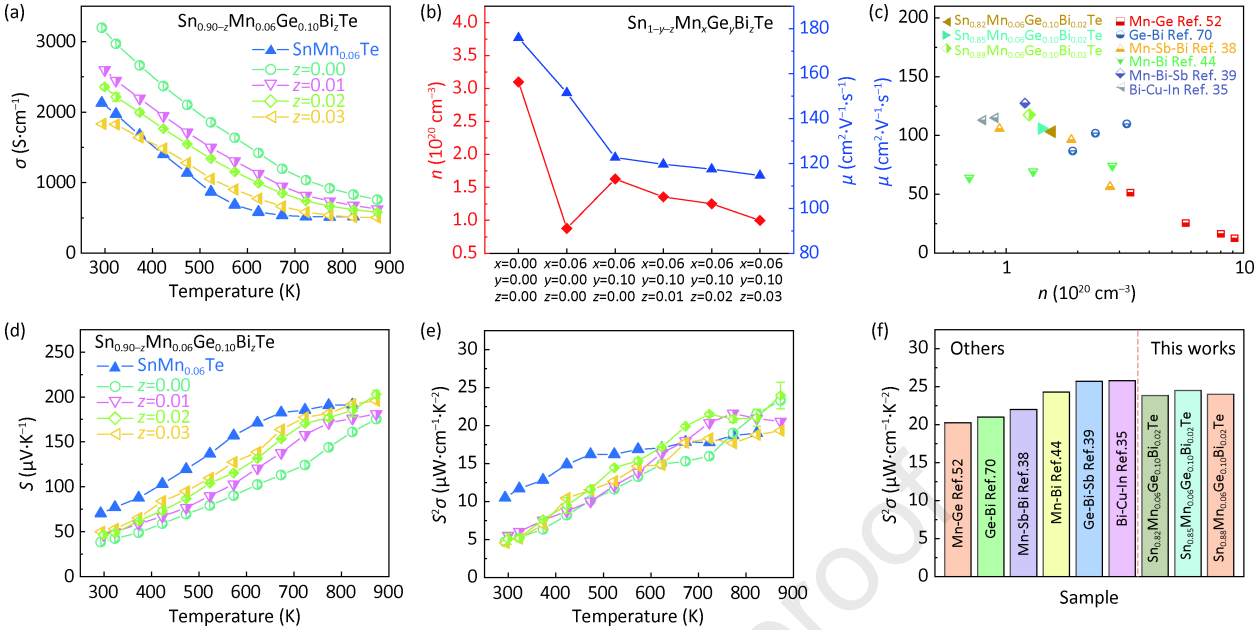

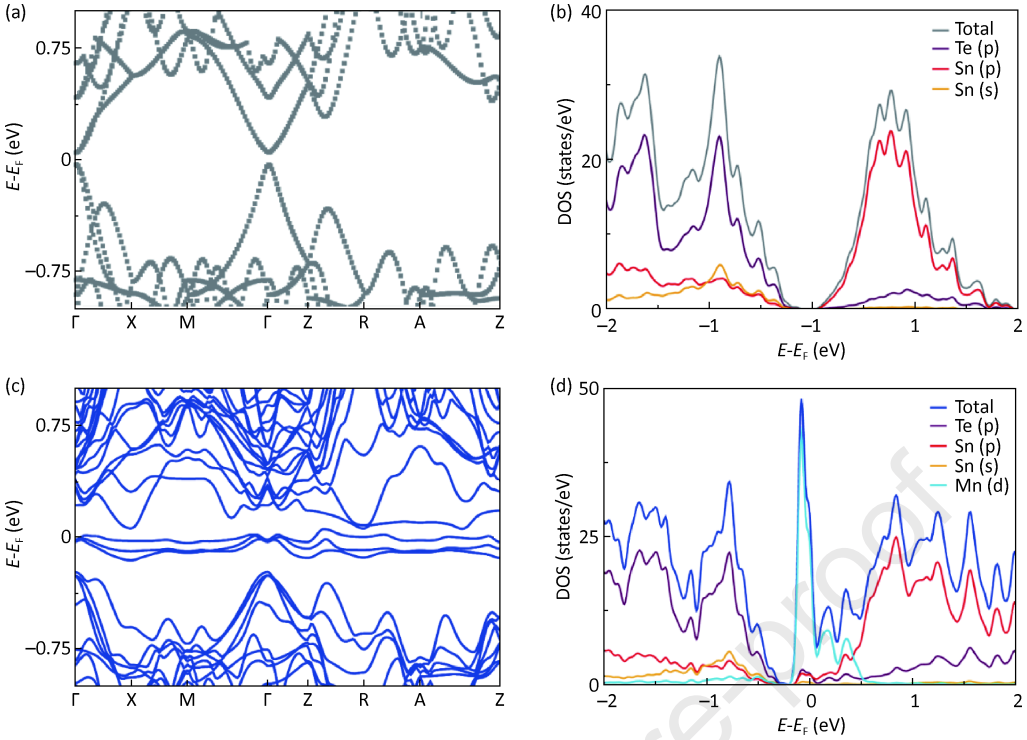

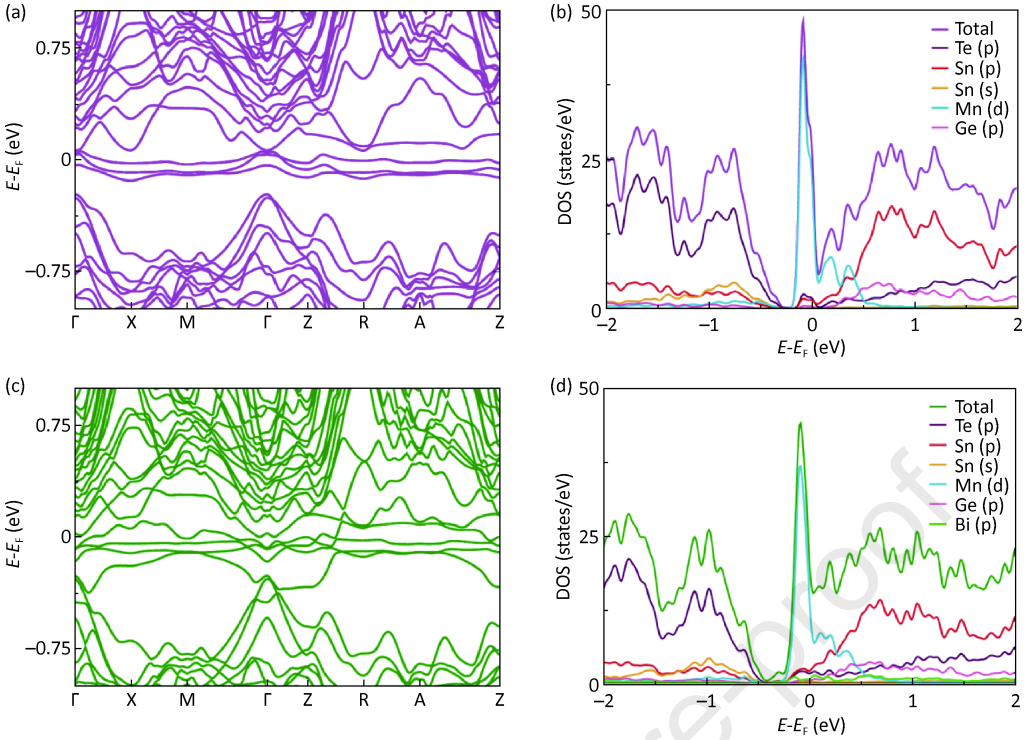

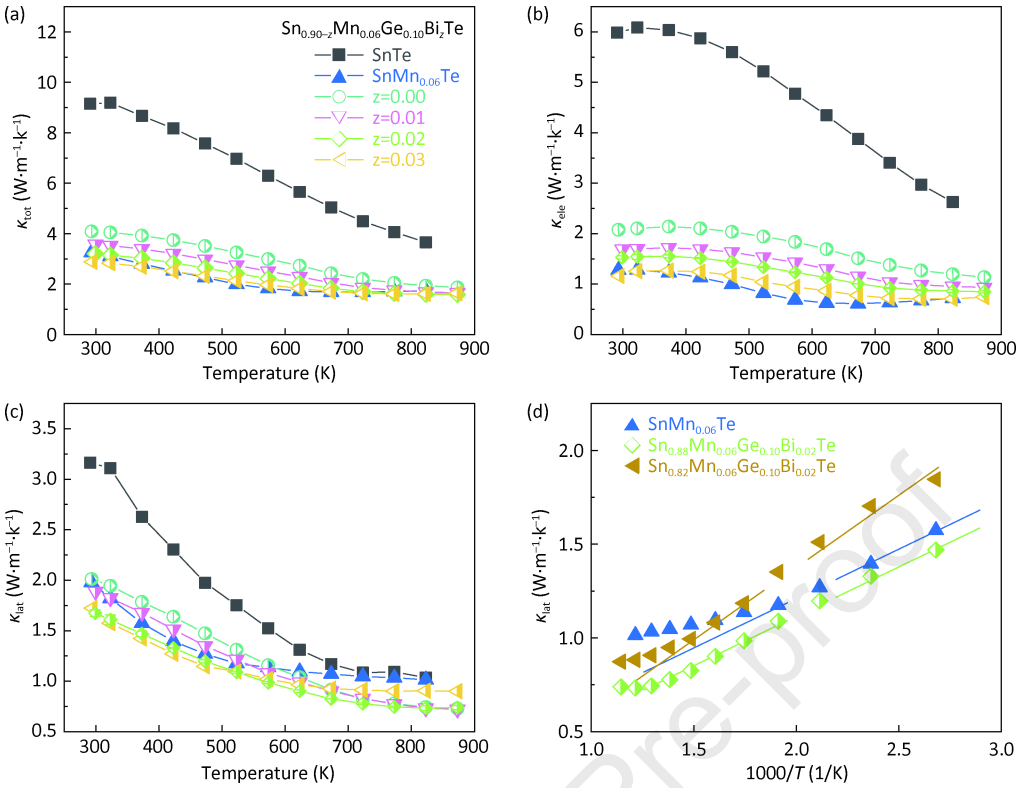

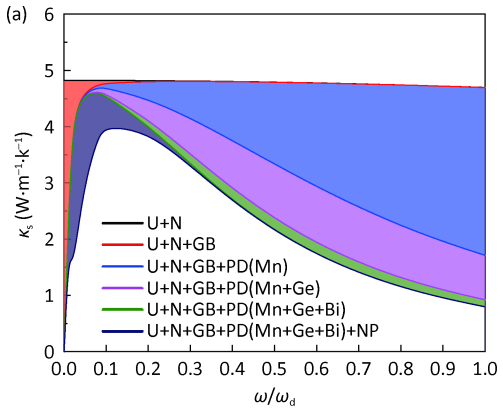

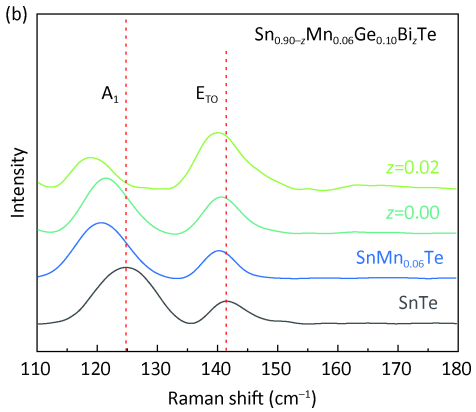

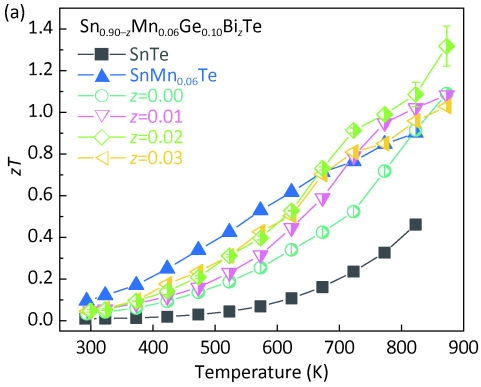

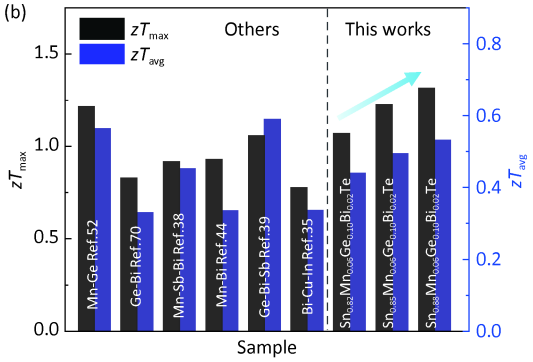

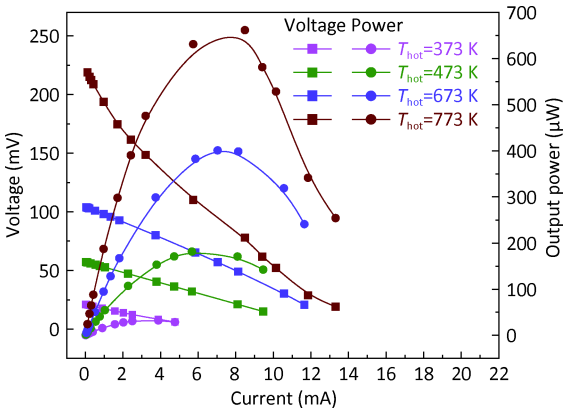

Highlights

- A $Sn_{0.88}Mn_{0.06}Ge_{0.10}Bi_{0.02}Te$ sample achieved a zT of 1.32 at 873K, outperforming conventionally tri-doped samples by ~23% in zT_{max}.
- Mn-Ge precipitates and coherently embedded nanostructures reduce lattice thermal conductivity.
- The two-pair thermoelectric generator recorded a maximum output power of 661 μW at ΔT = 485 K.

Declaration of interests

☒ The authors declare that they have no known competing financial interests or personal relationships that could have appeared to influence the work reported in this paper.

☐ The authors declare the following financial interests/personal relationships which may be considered as potential competing interests: